Enhancement and active mediation of near-field radiative heat transfer through multiple nonreciprocal graphene surface plasmons

Cheng-Long Zhou,[*] Lei Qu,[*] Yong Zhang, and Hong-Liang Yi ●[†]

School of Energy Science and Engineering, Harbin Institute of Technology, Harbin 150001, People's Republic of China
and Key Laboratory of Aerospace Thermophysics, Ministry of Industry and Information Technology,
Harbin 150001, People's Republic of China

Metasurfaces, the two-dimensional counterparts of three-dimensional metamaterials, have recently attracted much attention due to their interesting properties, such as negative refraction, hyperbolic dispersion, and the ability to manipulate the evanescent spectrum. In this work, we propose a theoretical model for near-field radiative heat transfer between two multilayered systems consisting of anisotropic metasurfaces. The choice of metasurface is graphene, with an adjustable drift current, since this provides an ideal platform to support a high density of modes around the plasmon frequency. In this configuration, multiple nonreciprocal surface plasmon polaritons are excited, providing a strong way for near-field energy transport. The resulting heat transfer, assisted by the graphene's multilayered structure and with a high drift-current velocity, is more than 36 times stronger than that of a graphene monolayer structure without a drift current for the same vacuum gap. By adjusting the vacuum gap and the thickness of a dielectric spacer, this enhanced effect can be modulated over a large range, and can even turn into a suppression. Our findings provide a powerful way to enhance and regulate energy transport, and in turn, open up a way to enrich the moiré physics inherent to the anisotropic optical properties of a metasurface.

I. INTRODUCTION

Compared with classical radiation [1,2], radiative heat transfer between two bodies can be significantly enhanced by bringing the bodies close enough to each other to allow tunneling of evanescent modes [3–5]. The huge radiative heat flux in the near field opens the door for various applications, like thermophotovoltaics [6–8], noncontact refrigeration [9–11], thermal rectification [12–14], and information memory [15]. Since maximal heat flux is of critical importance in these applications, continuous efforts have been devoted to maximizing such near-field radiative heat transfer (NFRHT) by controlling various material and structural parameters [16–20]. Typically, due to the predominant contribution to heat transfer from surface states, one obvious way to enhance heat transfer is to use multiple surface states. For example, periodic stacks of alternating subwavelength metal and dielectric layers enhance NFRHT through the surface modes of many surfaces [21]. However, high losses in metallic layers spoil the outstanding properties of surface waves, thereby weakening the enhancement of NFRHT excited by multilayer structures. Recently, metasurfaces, the two-dimensional analogs of three-dimensional metamaterials, have gained significant attention as a promising candidate for the lossless control of surface plasmon polaritons. Because of their preeminent optical properties, graphene sheets and other isotropic metasurfaces are widely used in multilayer structures to find different ways to enhance radiation heat transfer [22–26]. This strategy has resulted in sophisticated methods for regulating and enhancing near-field thermal radiation through the interaction of surface polaritons.

Nonetheless, up to now, metasurfaces in multilayer structures have been considered only as supports for isotropic surface polaritons. In the development of metamaterial fabrication, extensive studies have shown that the anisotropic polaritons of metasurfaces play a crucial role in NFRHT enhancement; such anisotropic polaritons include hyperbolic polaritons [27–29], nonreciprocal surface plasmons polaritons (NSPPs) [30], ellipse polaritons [31,32], and magnetoplasmon polaritons [33,34]. Thus, the accurate modulation of anisotropic surface polaritons in NFRHT, multilayered systems, with anisotropic metasurfaces, may be conducive to enhancing and adjusting radiative heat transfer. Unfortunately, due to a lack of understanding of the physics of multilayer anisotropic metasurfaces, there have been no studies on NFRHT in multilayered systems consisting of anisotropic metasurfaces. This is an area of research, therefore, in urgent need of attention, since it potentially contains many interesting phenomena that will lead to an increased number of tunable parameters in practical applications.

In this work, we focus on the NFRHT between two multilayers in the presence of anisotropic metasurfaces. Here, the anisotropic metasurfaces are composed of drift-biased graphene. The nonreciprocal surface plasmon polaritons supported by drift-biased graphene can greatly enhance NFRHT. Compared with the case of just two graphene sheets, such a

---

[*]These authors contributed equally to this work.
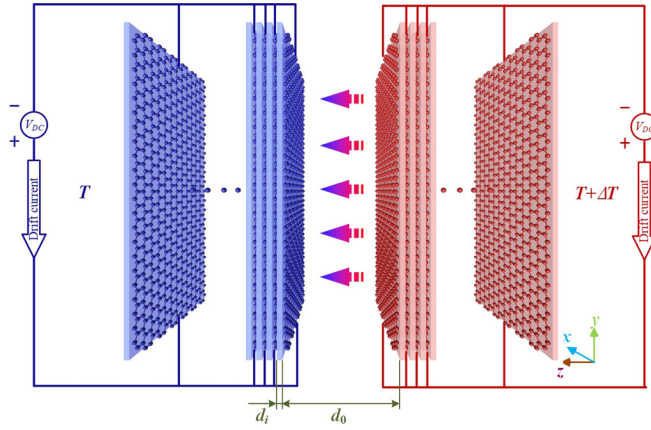[†]Corresponding author: yihongliang@hit.edu.cn

FIG. 1. Geometry of the multilayers composed of drift-biased graphene and a dielectric spacer. Here, d_0 and d_i are the widths of the middle vacuum gap and the thickness of dielectric spacer, respectively. The temperatures of the emitter and receiver are denoted $T + \Delta T$ and T, respectively.

multilayer anisotropic structure will not only support multiple nonreciprocal surface plasmon polaritons (MNSPPs), but will also exhibit significantly tunable features via varying the structure or optical parameters. This paper is structured as follows: In Sec. II, we introduce the geometry of our system and provide the expression for the heat flux through the multilayer drift-biased graphene. In Sec. III, we calculate the heat-transfer coefficient with respect to the number of graphene sheets, and discuss the coupled MNSPPs in the multilayered system by exploring the photon-tunneling probability. In Sec. IV, we compare the heat-transfer coefficient of the multilayered system with those of different structural parameters to provide guidance in choosing appropriate parameters for modulating NFRHT. The decay length of the MNSPPs is adopted to interpret the results. Finally, in Sec. V, we present a conclusion and suggestions for future work.

II. THEORETICAL ASPECTS

Figure 1 shows the near-field radiative heat transfer between multilayer systems in the presence of a direct drift

current along the graphene sheet, with drift velocity $\hat{v}_d = v_d \hat{y}$. Two periodic multilayer bodies are separated by a vacuum gap d_0. Each body consists of equally spaced graphene sheets separated by a dielectric spacer of thickness d_i. The dielectric layers are set as polystyrene. The number of graphene sheets in each body is denoted by N. The direct drift current is supplied by a voltage generator, with voltage V_{DC}. The right and left body are maintained at temperatures $T + \Delta T$ and T, respectively; T is equal to 300 K (room temperature) throughout this work. Since graphene is a good conductor, it does not affect the temperature distribution of the system due to Joule-heating arising from the drift current. For simplicity, we assume that the two bodies are mirror images of each other. Using the self-consistent quantum mechanical methods in Refs. [35,36], the conductivity of graphene with nonreciprocal effect can be defined as:

$$
\hat{\sigma}^d(\omega, v_d, k_x, k_y) = \begin{bmatrix} (\omega/\tilde{\omega})\sigma_{xx}^g(\tilde{\omega}, k_x, k_y) & (\omega/\tilde{\omega})\sigma_{xy}^g(\tilde{\omega}, k_x, k_y) \\ (\omega/\tilde{\omega})\sigma_{yx}^g(\tilde{\omega}, k_x, k_y) & (\omega/\tilde{\omega})\sigma_{yy}^g(\tilde{\omega}, k_x, k_y) \end{bmatrix}, \quad (1)
$$

where $\tilde{\omega} = \omega - k_y v_d$ is the Doppler-shifted frequency; and σ^g is the graphene conductivity in the absence of a drift-current bias, which is modeled by the Bhatnagar-Gross-Krook (BGK) approach derived in Ref. [37]. This BGK approach rigorously accounts for the intrinsic nonlocal response of graphene. Intuitively, reversing the propagation direction equates to changing the sign k_y and therefore the sign of the Doppler shift, i.e., $\sigma^d(\omega, k_y) \neq \sigma^d(\omega, -k_y)$ for $v_d \neq 0$. The relaxation time τ in the conductivity model is chosen as 3.5×10^{-13} s (following Ref. [38]). Note that the drift velocity close to the Fermi velocity ($v_f \approx 10^8$ cm/s) has been experimentally reported for graphene samples suspended in free space [39,40], and is selected as the maximum drift velocity. We thus have the relation $v_d = f v_f$, where f is the velocity ratio ranging from 0 to 0.9.

The theory derived below can be applied to any kind of multilayer two-dimensional (2D) anisotropic metasurface. In the framework of fluctuation electrodynamics, the radiative heat-transfer coefficient (RHTC) between two bodies of multilayer drift-biased graphene is given by [30]

$$
h = \int_0^\infty h_\omega(\omega) d\omega = \int_0^\infty \frac{\partial \Theta(\omega, T)}{\partial T} d\omega \int_{-\infty}^\infty \int_{-\infty}^\infty \frac{\xi(\omega, k_x, k_y)}{8\pi^3} dk_x dk_y \quad (2)
$$

where $\Theta(\omega, T) = \hbar\omega/[\exp(\hbar\omega/k_B T) - 1]$ is the mean energy of a Planck oscillator at angular frequency ω, and $\xi(\omega, k_x, k_y)$ is the photonic-transmission coefficient (PTC), which describes the probability of photons being excited by thermal energy [30]:

$$
\xi(\omega, k_x, k_y) = \begin{cases} \mathrm{Tr}\,[(\mathbf{I} - \mathbf{R}_2^*\mathbf{R}_2 - \mathbf{T}_2^*\mathbf{T}_2)\,\mathbf{D}\,(\mathbf{I} - \mathbf{R}_1\mathbf{R}_1^* - \mathbf{T}_1^*\mathbf{T}_1)\mathbf{D}^*], & k < k_0 \\ \mathrm{Tr}\,[(\mathbf{R}_2^* - \mathbf{R}_2)\,\mathbf{D}\,(\mathbf{R}_1 - \mathbf{R}_1^*)\mathbf{D}^*]e^{-2|k_z|d}, & k > k_0 \end{cases} \quad (3)
$$

for propagating ($k < k_0$) and evanescent ($k > k_0$) waves where $k = \sqrt{k_x^2 + k_y^2}$ is the surface parallel wave vector and $k_0 = \omega/c$ is the wave vector in vacuum. $k_z = \sqrt{k_0^2 - k^2}$ is the tangential wave vector along the z direction in vacuum, and $*$ signifies the complex conjugate. The 2×2 matrix $\mathbf{D}$ is defined as $\mathbf{D} = (\mathbf{I} - \mathbf{R}_1\mathbf{R}_2 e^{2ik_z d})$, which describes the usual Fabry-Perot-like denominator, resulting from multiple scattering between emitter and receiver [30]. The reflection matrix $\mathbf{R}$ is a 2×2 matrix in the polarization representation.

In this section, a generalized 4×4 T-matrix formalism for arbitrary anisotropic 2D layers is developed, from which the general relations for the surface wave dispersions and reflection matrix $\mathbf{R}$ are derived. Let us first consider a single anisotropic metasurface at the interface between two semi-infinite media. Using the homogenization approach, the electromagnetic (EM) response of such a metasurface, in general, can be described by a fully populated conductivity tensor $\hat{\sigma}''$ in the wave-vector

space. Moreover, $\hat{\sigma}''$ denotes the conductivity tensor in the wave-vector space [41]:

$$\hat{\sigma}'' = \begin{pmatrix} \sigma''_{xx} & \sigma''_{xy} \\ \sigma''_{yx} & \sigma''_{yy} \end{pmatrix} = \frac{1}{k^2} \begin{pmatrix} k_x^2 \sigma_{xx} + k_y^2 \sigma_{yy} + k_x k_y (\sigma_{xy} + \sigma_{yx}) & k_x^2 \sigma_{xy} - k_y^2 \sigma_{yx} + k_x k_y (\sigma_{yy} - \sigma_{xx}) \\ k_x^2 \sigma_{yx} - k_y^2 \sigma_{xy} + k_x k_y (\sigma_{yy} - \sigma_{xx}) & k_x^2 \sigma_{yy} + k_y^2 \sigma_{xx} - k_x k_y (\sigma_{xy} + \sigma_{yx}) \end{pmatrix}. \tag{4}$$

Following Refs. [42–44] let us write separately the EM field of the p-polarized (TM) and s-polarized (TE) components of the EM wave, which then will be mixed by the nondiagonal response of a metasurface. The p waves, with the magnetic field perpendicular to the incidence plane, possess the EM-field components $E_p = \{E_x, 0, E_z\}$, $H_p = \{0, H_y, 0\}$. For the s waves, with the electric field perpendicular to the incidence plane, the EM-field components are $E_s = \{0, E_y, 0\}$, $H_s = \{H_x, 0, H_z\}$. Substituting the p and s waves into the boundary conditions of the metasurface [45], one obtains the 4×4 T matrix, which gives the relation between all the electric-field components and the

magnetic field components in the media above and below the metasurface:

$$\begin{bmatrix} H_{p1}^+ \\ H_{p1}^- \\ E_{s1}^+ \\ E_{s1}^- \end{bmatrix} = \hat{T}_{1 \to 2} \begin{bmatrix} H_{p2}^+ \\ H_{p2}^- \\ E_{s2}^+ \\ E_{s2}^- \end{bmatrix}. \tag{5}$$

The signs of $+$ and $-$ represent a forward and backward propagating wave, respectively. Subscripts 1 and 2 represent the media above and below the metasurface, respectively. $\hat{T}_{1 \to 2}$ is defined as

$$\hat{T}_{1 \to 2} = \frac{1}{2} \begin{bmatrix} \frac{k_{z2}}{\varepsilon_2} \begin{bmatrix} \frac{\varepsilon_1}{k_{z1}} + \frac{\varepsilon_2}{k_{z2}} + \frac{\sigma''_{xx}}{\omega \varepsilon_0} & -\frac{\varepsilon_1}{k_{z1}} + \frac{\varepsilon_2}{k_{z2}} - \frac{\sigma''_{xx}}{\omega \varepsilon_0} \\ -\frac{\varepsilon_1}{k_{z1}} + \frac{\varepsilon_2}{k_{z2}} + \frac{\sigma''_{xx}}{\omega \varepsilon_0} & \frac{\varepsilon_1}{k_{z1}} + \frac{\varepsilon_2}{k_{z2}} - \frac{\sigma''_{xx}}{\omega \varepsilon_0} \end{bmatrix} & \sqrt{\frac{\mu_0}{\varepsilon_0}} \sigma''_{xy} \begin{bmatrix} 1 & 1 \\ 1 & 1 \end{bmatrix} \\ \sqrt{\frac{\mu_0}{\varepsilon_0} \frac{k_{z2}}{\varepsilon_2 k_{z1}}} \sigma \sigma''_{yx} \begin{bmatrix} 1 & -1 \\ -1 & 1 \end{bmatrix} & \begin{bmatrix} 1 + \frac{k_{z2}}{k_{z1}} + \frac{\omega \mu_0 \sigma''_{yy}}{k_{z1}} & 1 - \frac{k_{z2}}{k_{z1}} + \frac{\omega \mu_0 \sigma''_{yy}}{k_{z1}} \\ 1 - \frac{k_{z2}}{k_{z1}} - \frac{\omega \mu_0 \sigma''_{yy}}{k_{z1}} & 1 + \frac{k_{z2}}{k_{z1}} - \frac{\omega \mu_0 \sigma''_{yy}}{k_{z1}} \end{bmatrix} \end{bmatrix}, \tag{6}$$

where ε_1 and ε_2 represent the dielectric constant of the media above and below the metasurface, respectively; and k_{z1} and k_{z2} are the tangential wave vectors along the z direction in the media above and below the metasurface, respectively. In general, for any 4×4 T matrix that links all the electric-field components in the first layer with those in the Nth layer,

$$\begin{bmatrix} H_{p1}^+ \\ H_{p1}^- \\ E_{s1}^+ \\ E_{s1}^- \end{bmatrix} = \begin{bmatrix} T_{11} & T_{12} & T_{13} & T_{14} \\ T_{21} & T_{22} & T_{23} & T_{24} \\ T_{31} & T_{32} & T_{33} & T_{34} \\ T_{41} & T_{42} & T_{43} & T_{44} \end{bmatrix} \begin{bmatrix} H_{pN}^+ \\ H_{pN}^- \\ E_{sN}^+ \\ E_{sN}^- \end{bmatrix}. \tag{7}$$

The reflection matrix **R** is defined and expressed in terms of the T-matrix elements as follows [46]:

$$r_{pp} = \left. \frac{H_{p1}^-}{H_{p1}^+} \right|_{E_{s1}^+ = 0} = \frac{T_{21} T_{33} - T_{23} T_{31}}{T_{11} T_{33} - T_{13} T_{31}},$$

$$r_{ps} = \left. \frac{E_{s1}^-}{H_{p1}^+} \right|_{E_{s1}^+ = 0} = \frac{T_{41} T_{33} - T_{43} T_{31}}{T_{11} T_{33} - T_{13} T_{31}},$$

$$r_{sp} = \left. \frac{H_{p1}^-}{E_{s1}^+} \right|_{H_{p1}^+ = 0} = \frac{T_{11} T_{23} - T_{13} T_{21}}{T_{11} T_{33} - T_{13} T_{31}},$$

$$r_{ss} = \left. \frac{E_{s1}^-}{E_{s1}^+} \right|_{H_{p1}^+ = 0} = \frac{T_{11} T_{43} - T_{13} T_{41}}{T_{11} T_{33} - T_{13} T_{31}}. \tag{8}$$

The formulism developed above can be easily generalized for arbitrary multilayer systems by multiplying the T matrices corresponding to each layer. For a multilayer metasurface consisting of N 2D layers with effective conductivity tensors

$\hat{\sigma}''_j$ ($j = 1, 2, ..., N$), one obtains a 4×4 T matrix, which gives the relations between all the electric-field components in the multilayer metasurface:

$$\begin{bmatrix} H_{p1}^+ \\ H_{p1}^- \\ E_{s1}^+ \\ E_{s1}^- \end{bmatrix} = \hat{T}_{1 \to N} \begin{bmatrix} H_{pN}^+ \\ H_{pN}^- \\ E_{sN}^+ \\ E_{sN}^- \end{bmatrix}, \tag{9}$$

where

$$\hat{T}_{1 \to N} = \hat{T}_{1 \to 2} \hat{T}_{d_{i,1}} \hat{T}_{2 \to 3} \hat{T}_{d_{i,2}} ... \hat{T}_{d_{i,N-1}} \hat{T}_{N \to N-1} \hat{T}_{d_{i,N}}, \tag{10}$$

where $\hat{T}_{j \to j+1}$ is obtained from $\hat{T}_{1 \to 2}$ [Eq. (6)] by replacing $\hat{\sigma}''_1$ with $\hat{\sigma}''_j$, and $\hat{T}_{d_{i,j}}$ is the T matrices for a wave propagating through the vacuum between two adjacent 2D layers of thickness $d_{i,j} (j = 1, 2, ..., N)$:

$$T_{d_{i,j}} = \begin{bmatrix} e^{-ik_{z0}d_{i,j}} & 0 & 0 & 0 \\ 0 & e^{ik_{z0}d_{i,j}} & 0 & 0 \\ 0 & 0 & e^{-ik_{z0}d_{i,j}} & 0 \\ 0 & 0 & 0 & e^{ik_{z0}d_{i,j}} \end{bmatrix}. \tag{11}$$

The dispersion of the collective surface waves in such an N-layer system can be found when the denominators of the reflection coefficients is zero:
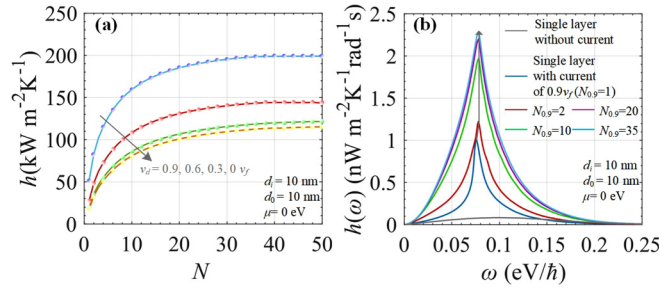
$$T_{11} T_{33} - T_{13} T_{31} = 0. \tag{12}$$

FIG. 2. (a) Radiative heat-transfer coefficient h as a function of N between drift-biased graphene/polystyrene multilayers, with different drift-current velocities. (b) Comparison of the spectral RHTC for systems with $N = 1$, 2, 10, 20, and 35 at a high drift-current velocity of $0.9v_f$. The gray lines shown in (b) correspond to the results obtained by modeling the system as monolayer graphene without a drift-current. The parameters are $d_i = d_0 = 10$ nm, $T = 300$ K, and $\mu = 0$ eV.

Using a T matrix allows us to obtain all necessary characteristics (the reflection and the dispersion relations) using Eqs. (5)–(12).

III. SIGNIFICANT ENHANCEMENT OF RADIATIVE HEAT TRANSFER BETWEEN TWO PERIODIC MULTILAYERS BASED ON MNSPPs

Based on the framework above, we calculate the RHTC using Eq. (2) for multilayer-system configurations, as shown in Fig. 1. As a concrete example, we set the thickness d_i of the dielectric spacer to the width of the vacuum gap d_0, i.e., $d_i = d_0 = 10$ nm; the chemical potential of graphene is set to $\mu = 0$ eV, and the RHTC is evaluated at room temperature (300 K). The drift currents of each layer are the same. These parameters are used throughout the paper unless otherwise mentioned. Note that "monolayer" in the following means that each body consists of a monolayer drift-biased graphene sheet.

Figure 2(a) shows h as a function of the number of drift-biased graphene sheets N for multilayers with different drift-current velocities. We find that h increases as N increases and is more sensitive to change in N when N is relatively small ($N < 20$). For a zero-current system, more specifically, for $N = 1$ and 20, h increases from 17.1 to 102.5 kW m^{-2} K^{-1}. As the number of sheets increases to a high value, for example, $N = 50$, h no longer changes with N, remaining constant at 115.3 kW m^{-2} K^{-1}, 6.74 times larger than that of the monolayer—this indicates an enhancement of heat transfer in the multilayers. Figure 2(a) shows that with increasing drift-current velocity, the near-field RHTCs of the multilayer system with different numbers are enhanced by the drift current, and no saturation behavior is observed. Moreover, the curves with different drift velocities show a similar trend as the number of graphene layers increases. However, clearly, enhancement of the RHTC, with a high drift-current velocity, is more sensitive to change in N when N is small. When the number of graphene layers reaches 50, the maximum RHTC of the multilayer system is 198.9 kW m^{-2} K^{-1} at a high current velocity of $0.9 v_f$—this is an order of magnitude greater

than the near-field heat transfer of the zero-current monolayer system shown in Fig. 2(a). Figure 2(a) shows that the radiative heat transfer of the nonreciprocal anisotropic multilayers is larger than that of isotropic multilayered systems ($v_d = 0$) in a different number of graphene layers. Based on the above comparison, we infer there must be strong sheet couplings in the nonreciprocal anisotropic multilayers, which contribute to heat-transfer enhancement.

In Fig. 2(b), we compare spectral RHTCs with a high drift-current velocity of $0.9v_f$ for $N = 1$, 2, 10, 20, and 35. For large N, the curve has a high value over the whole spectral range. The peak value shifts slightly to a higher angular frequency. The maximum of a spectral RHTC is blueshifted from 0.076 eV$/\hbar$ for $N = 1$ to around 0.078 eV$/\hbar$ for $N = 35$. The maximum also increases drastically with the number of graphene layers, reaching its highest value of 2.29 nW m^{-2} K^{-1} rad^{-1} s. This explains why the RHTC in Fig. 2(a) increases as the number of graphene layers increases. To visualize the significant enhancement in the RHTC, Fig. 2(b) shows the spectral RHTC between two zero-current monolayer graphene sheets. The system composed of zero-current monolayer graphene only has a maximum of 0.083 nW m^{-2} K^{-1} rad^{-1} s at a frequency of 0.1 eV$/\hbar$. In contrast, the nonreciprocal anisotropic multilayers yield a significant enhancement in the spectral heat flux, hence also providing a huge enhancement in total heat transfer.

The mechanism for enhanced heat transfer can be elucidated using the contours of the PTC $\xi(\omega, k_x, k_y)$ in the wave-vector plane in Fig. 3. The wave vector is normalized by k_0. Figures 3(a)–3(d) show the enhanced photon tunneling probability of the nonreciprocal anisotropic multilayers. Figure 3(a) shows the PTC for a typical scenario of NFRHT between two suspended graphene sheets [27]. Both the left and right vacuum-graphene interfaces support evanescent waves, which decay exponentially along the direction perpendicular to the interfaces. Figure 3(a) shows evanescent waves from each interface interacting with each other, leading to splitting of the resonance into antisymmetric (inner circle) and symmetric (outer circle) modes, making a major contribution to the high near-field heat flux [30]. As is well known, the graphene sheet supports isotropic SPPs due to collective charge oscillations coupled to light. Under a voltage bias, the collective charge oscillations are strongly affected by the dragging effect of drifting charges, which causes guided waves to exhibit asymmetric effects, and in turn, presents NSPPs. Figure 3(b) shows that when the drift velocity reaches $0.9v_f$, the maximum wave vector of the bright branches in the bottom k_y quadrants approach $-1200k_0$. Moreover, compared with those in the absence of a drift current, as shown in Figs. 3(a) and 3(b), NSPPs also lead to a significantly wider bright branch of plasmons with drift current in the bottom k_y quadrant (propagating towards these drifting charges). This is why NSPPs can induce strong radiative heat transfer.

As more layers are stacked, due to newly added drift-biased graphene interfaces, multiple reflections and wave interference within the multilayered structure become more intense, producing photonic-transmission coefficient contours with more branches. As the two bodies composed of bilayer nonreciprocal metasurfaces are brought near one another, coupling of the MNSPPs produces newly symmetric and antisymmetric
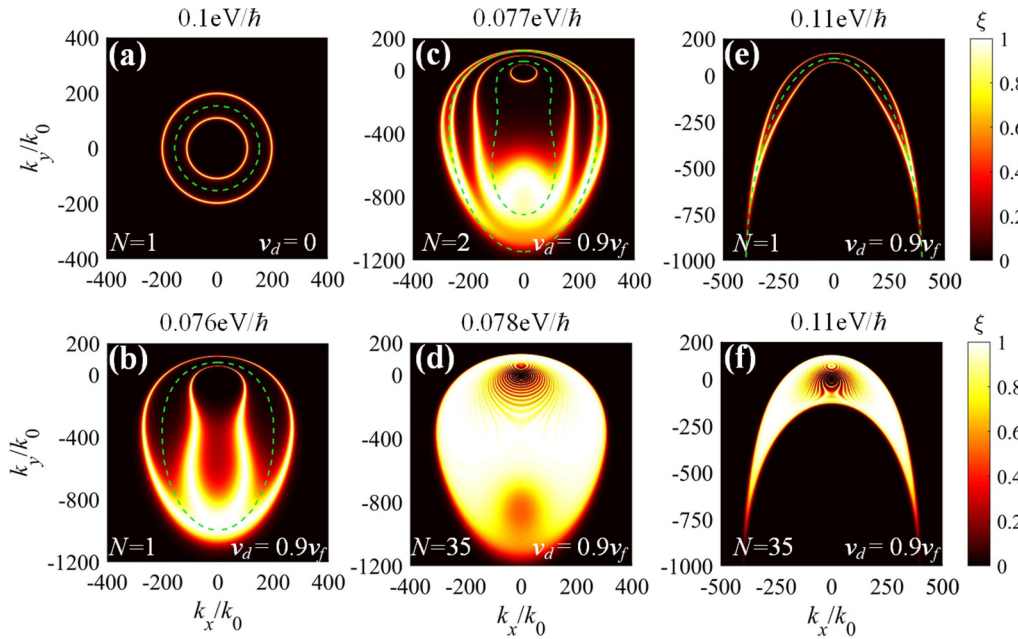
FIG. 3. Photonic-transmission coefficient contours at respective peak frequencies for monolayer graphene with different drift-current velocities: (a) $v_d = 0$ and (b) $v_d = 0.9v_f$. Photonic-transmission coefficient contours at peak frequencies and a high drift-current velocity of $0.9v_f$ for drift-biased graphene/polystyrene multilayers with different numbers of layers: (c) $N = 2$ and (d) $N = 35$. Photonic-transmission coefficient contours at a peak frequency of $0.11\,\text{eV}/\hbar$ and a high drift-current velocity of $0.9v_f$ for drift-biased graphene/polystyrene multilayers with different numbers: (e) $N = 1$ and (f) $N = 35$. The green dashed lines denote the dispersion relations calculated by Eq. (12) for the multilayers.

branches in the wave-vector space, meaning the number of total branches now equals 4, as indicated in Fig. 3(c). Surfaces situated away from the middle gap provide additional surface states, serving as a "relay" that enables surfaces even farther away from the gap to contribute to heat transfer. In Fig. 3(c), the green dotted lines are nicely located between the bright branches, which unambiguously demonstrates that the MNSPPs of bilayer nonreciprocal metasurfaces predominate NFRHT in our system. Remarkably, when the number of system layers increases to 35 in Fig. 3(d), due to the coupling of many surface states, the contours of the photonic-transmission coefficients evolve into a large, bright, egg-shaped area, with a PTC value close to 1—this greatly enhances radiative heat transfer. As a result, a significant enhancement in near-field heat transfer is achieved through coupling of a many surface state from multiple nonreciprocal interfaces.

When the number of graphene layers is 1, the spectral RHTC curve at $0.9v_f$ appears as the sharp peak in Fig. 2(b). The spectral RHTC quickly reaches as high as $1.05\,\text{nW}\,\text{m}^{-2}\,\text{K}^{-1}\,\text{rad}^{-1}\,\text{s}$ at a frequency of $0.076\,\text{eV}/\hbar$, and decreases rapidly as the frequency ω further increases. In order to explain the mechanism, we plot the photonic-transmission coefficient for a frequency of $0.11\,\text{eV}/\hbar$. Clearly, there is a lack of unidirectional wave vector appearing in the bottom k_y quadrants of Fig. 3(e); i.e., NSPPs are no longer closed. The open shape of NSPPs appears due to the intrinsic nonlocal response of graphene, as the finite velocity of electrons v_f cannot match the increasing velocity inherent to plasmon variations [47]. This is because when a high drift-current velocity is applied to the system, the NSPPs are incapable of significantly increasing the heat flux

of the structure. Fortunately, as the number of graphene layers increases, this rapid decay of spectral RHTC caused by intrinsic nonlocal response is moderately relieved. In Fig. 3(f), although the increase in the number of graphene layers does not prevent formation of an MNSPP open shape, additional surface states form a large bright band, which reduces attenuation of the spectral RHTC; this reduction in attenuation, in turn, further enhances radiative heat transfer.

According to the above analysis, for a high drift-current velocity, when the number of graphene layers is greater than 35, the RHTC no longer increases significantly with the number of graphene layers. Therefore, the number of graphene layers should be fixed at 35 in subsequent work, unless otherwise specified. It is well known that the chemical potential μ represents an adjustable parameter, allowing the active tuning of the optical properties of graphene. We now examine the influence of chemical potential on the enhanced effect in the RHTC between nonreciprocal multilayer metasurfaces. The results for the parameters $d_0 = 10\,\text{nm}$, $d_i = 10\,\text{nm}$, and $N = 35$ are plotted in Fig. 4. Such a dependence of RHTC, controlled by different chemical potentials, on drift-current velocity is shown in Fig. 4(a)—with increasing μ, the RHTC decreases. The positive correlation between the RHTC and drift-current velocity is greatly suppressed with increasing chemical potential, especially for $\mu \geqslant 0.4\,\text{eV}$. The influence of MNSPPs on the RHTC is most pronounced for low chemical potentials. For the system with a zero chemical potential, h increases from $110.2\,\text{kW}\,\text{m}^{-2}\,\text{K}^{-1}$ for $v_d = 0$ to $195.0\,\text{kW}\,\text{m}^{-2}\,\text{K}^{-1}$ for $v_d = 0.9v_f$, an increase of 1.77 times. In contrast, for the system at a chemical potential of $0.6\,\text{eV}$,
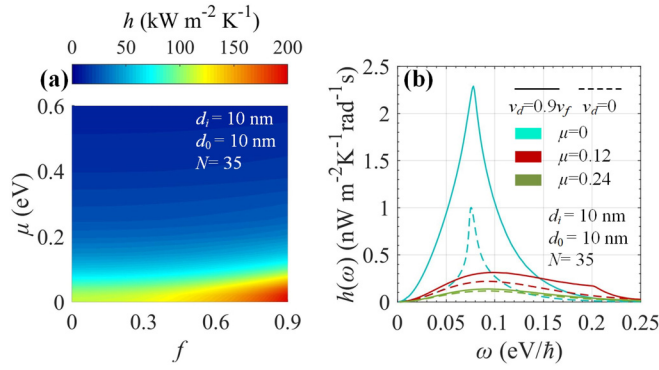
FIG. 4. (a) RHTC and (b) spectral RHTC with $v_d = 0$ and $v_d = 0.9v_f$ for different chemical potentials of 0, 0.12, and 0.24 eV. The solid and dotted lines shown in (b) correspond to the results obtained by applying a drift velocity of $0.9v_f$ and zero current, respectively.

FIG. 5. Heat-transfer enhancement ratio R between drift-biased multilayers and zero-current monolayer as a function of drift-current velocity and chemical potential.

the increase in the RHTC from the zero-current system to the high-current system is negligible—merely from 10.1 to $10.7 \, \mathrm{kW \, m^{-2} \, K^{-1}}$.

To explore the physical mechanism underlying the RHTC for different chemical potentials, spectral results for different μ with $v_d = 0$ and $0.9v_f$ are given in Fig. 4(b). When the drift-biased graphene multilayers are given a high chemical potential, the spectral peak significantly decreases, which in turn causes the RHTC to decrease. For $\mu = 0.12 \, \mathrm{eV}$, the peak value for $0.9v_f$ is only $0.22 \, \mathrm{nW \, m^{-2} \, K^{-1} \, rad^{-1}}$ s at a frequency of $0.092 \, \mathrm{eV}/\hbar$. Moreover, when the frequency reaches $0.22 \, \mathrm{eV}/\hbar$, the spectral RHTC with $\mu = 0.12 \, \mathrm{eV}$ and $0.9v_f$ drops sharply due to the open mode of MNSPPs generated by the intrinsic nonlocal response of graphene. According to Ref. [29], as the chemical potential of graphene increases, the MNSPPs are excited only by high photonic energy. However, the contribution of MNSPPs to the RHTC at high frequencies is negligible due to the exponential decay of the mean energy of a Planck oscillator at room temperature. Therefore, in Fig. 4(b), the maxima of the spectral RHTC greatly decrease with increasing chemical potential. Consequently, as the chemical potential increases, the ability of the drift current to enhance the spectral RHTC peak gradually decreases. When the chemical potential reaches 0.24 eV, the maximum of the spectral RHTC only increase from $0.12 \, \mathrm{nW \, m^{-2} \, K^{-1} \, rad^{-1}}$ s for zero current to $0.14 \, \mathrm{nW \, m^{-2} \, K^{-1} \, rad^{-1}}$ s for $v_d = 0.9v_f$ in Fig. 4(b).

To characterize the enhanced NFRHT from nonreciprocal anisotropic multilayers, we define the heat-transfer enhancement ratio R for heat transfer between drift-biased multilayers and a zero-current monolayer as a function of drift current and chemical potential, i.e., $R = h_{35}(\mu, v_d)/h_1(\mu, 0)$. Figure 5 shows clearly that, as the drift-current velocity increases, R increases. Interestingly, maximum R does not appear in the area of zero chemical potential; instead, R is maximal when $\mu \approx 0.09 \, \mathrm{eV}$. The maximum enhancement in heat transfer between drift-biased multilayers and a zero-current monolayer is about 20 times, as shown in Fig. 5. Near-field heat transfer is significantly enhanced by contributions from multiple nonreciprocal surface plasmon polaritons.
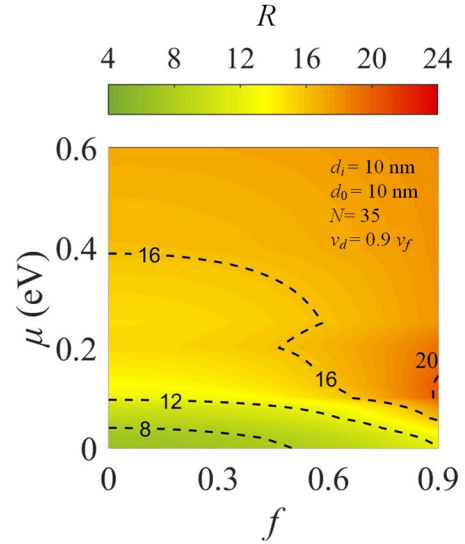
IV. EFFECT OF THE MULTILAYERED STRUCTURE ON RADIATIVE HEAT TRANSFER

Our work has revealed so far that MNSPPs provided by the drift-biased multilayered system greatly enhance the NFRHT. Nevertheless, the above analysis is conducted with only a fixed thickness of dielectric spacer and a fixed vacuum gap. In this section, we further study NFRHT in this multilayered system by adjusting the vacuum gap d_0 and the thickness d_i of dielectric spacer. This work will provide guidance for researchers to choose an appropriate multilayered structure to obtain maximum heat transfer at the nanoscale. Note that the number of graphene layers should be fixed at 35, as discussed earlier in Sec. III.

Figure 6(a) shows that for a chemical potential of 0.09 eV and a drift-current velocity of $0.9v_f$, the radiative heat-transfer coefficients h are functions of the vacuum gap for multilayers of thickness $d_i = 10, 30, 50, 70$, and 90 nm. For comparison, we also show h of the monolayer with drift-current velocities of 0 and $0.9v_f$. As d_0 increases from 2 to 1000 nm, the drift-biased multilayered systems with different d_i exhibit a trend of
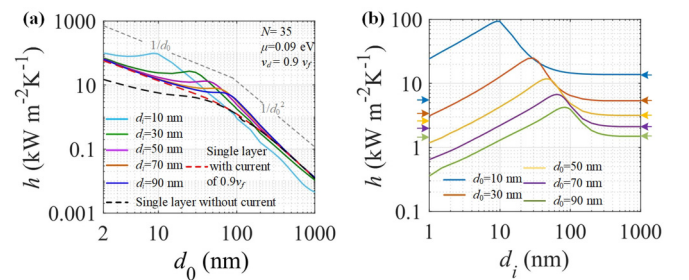

FIG. 6. Radiative heat-transfer coefficient h of the multilayers (a) with different vacuum-gap thicknesses d_0, and (b) for different dielectric spacers of thickness d_i. In (b), the short color bars on the right and left indicate h of the monolayer at $0.9v_f$ and $0v_f$, respectively.
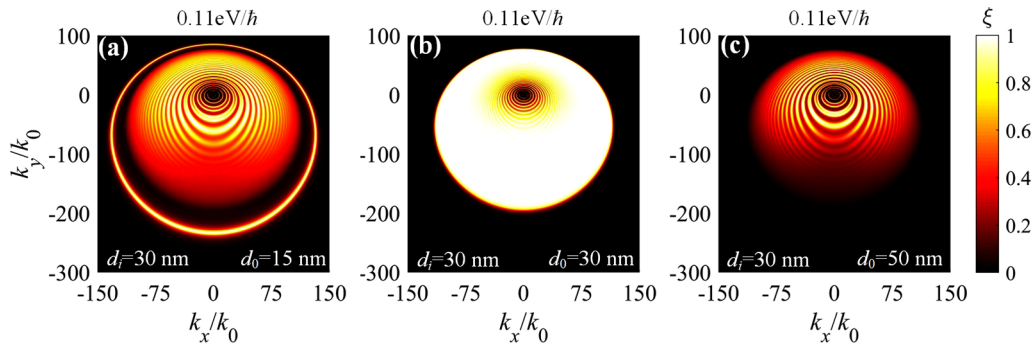
FIG. 7. Photonic-transmission coefficient contours for multilayers with three different vacuum gaps at a frequency of $0.11\,\mathrm{eV}/\hbar$: (a) $d_0 = 15$ nm, (b) $d_0 = 30$ nm, and (c) $d_i = 50$ nm for $N = 35$. The thickness of dielectric spacer is fixed at $d_i = 30$ nm.

nonmonotonous decrease. A local transition point at $d_0 \approx d_i$ is observed. When d_i is small, a peak in h appears at the local transition point, near which h of the multilayered system is much higher than that of the monolayer system at zero current. After the local transition point, h decreases rapidly and, interestingly, shows the well-known $1/d_0^2$ dependency similar to the bulk system. For further insight into the non-monotonic behavior, Fig. 7 shows the photonic-transmission coefficient. The vacuum gap $d_i = 30$ nm and dielectric-spacer thicknesses $d_0 = 15$, 30, and 50 nm are shown in Figs. 7(a)–7(c). Due to the weak attenuation of the evanescent wave in the small vacuum gap, when the vacuum gap is 15 nm, the multilayer structure supports photon tunneling at the larger wave-vector region. Figure 7(a) shows clearly that a bright band is formed in the larger wave-vector range. However, when d_i is smaller than d_0, due to the mismatch of vacuum gap and dielectric-spacer thicknesses, interlayer coupling in the multilayer structure is weak, resulting in weakening of the MNSPPs inside the outermost bright band. As the vacuum gap increases to 30 nm, the outermost bright band becomes filtered. Fortunately, the vacuum gap and the dielectric-spacer thicknesses now match well. Strong interlayer coupling in the multilayer structure forms a large, bright, egg-shaped area, with a PTC value close to 1 in wave-vector space in Fig. 7(b). Therefore, the NFRHT for $d_0 = 30$ nm is higher than the NFRHT for $d_0 = 15$ nm, as shown in Fig. 6(a). As the vacuum gap further increases, its filtering characteristics significantly attenuate the evanescent wave of the multilayer structure. Figure 7(c) shows that, compared with the photonic-transmission coefficient at smaller vacuum gap, the wave-vector range of the bright band is further compressed and its brightness is also reduced, which in turn decreases the NFRHT.

To visualize the effects of dielectric spacer thickness d_i on h, Fig. 6(b) shows the h curves as a function of d_i for different vacuum gaps of $d_0 = 10$, 30, 50, 70, and 90 nm. A local maximum of the RHTC is observed when d_i is close to d_0. The values h pointed to by the short color bars on the right border-line represent the corresponding of the monolayer with $0.9v_f$. These curves of Fig. 6(b) show that as d_i tends to infinity, the multilayer behaves as a monolayer. Physically, this result can be explained by analyzing the radiation penetration depth δ. In the electrostatic limit, the penetration depth of an evanescent wave is given by $1/(2\mathrm{Im}\{k_z\})$. As the thickness d_i between adjacent layers of drift-biased graphene increases, contributions for heat transfer from graphene sheets away from the

vacuum gap diminish due to loss of the evanescent wave. Consequently, the multilayer body behaves as a surface. Heat transfer maximizes when d_0 is comparable to the layer thickness d_i, similar to the optimum condition for the geometry of superlens effect. The mechanism behind this phenomenon is the relay mechanism [48]. This relay mechanism has been applied in the control of near-field heat transfer in an isotropic three-body system and in an isotropic multilayer system [49]. These results of Fig. 6 also confirm that the relay mechanism is also applicable in an anisotropic multilayer metasurface system. Hence, a significant enhancement is observed due to the coupling of MNSPPs. When d_i is much smaller than d_0, the heat-transfer rate is significantly suppressed; i.e., the enhanced effect on the RHTC of the nonreciprocal multilayers is destroyed. As shown in Fig. 6(b), the values h pointed to by the short color bars on the left borderline represent the NFRHT of the monolayer at zero current—as d_0 approaches several folds of d_i, the surface characteristics of the multilayers become more like those of a graphite film. In fact, the suppressed effect of heat transfer is especially prominent for a very compact drift-biased multilayer.

The photon-tunneling probabilities $\xi(\omega, k_x, k_y)$ of the multilayers are used to gain further insight into the physics behind the influence of dielectric-spacer thickness on radiative heat transfer. A vacuum gap of $d_0 = 30$ nm and dielectric-spacer thicknesses of $d_i = 1$, 29, and 300 nm are considered in Figs. 8(a)–8(c), respectively. Clearly, as $d_i < d_0$ for $N = 2$, at multilayered structure, the surface states interfere with one another, weakening the coupling of surface states. There are only two bright-band branches, i.e., the characteristics of the graphene bilayer are like those of the bulk structure. The single green dotted line is located between the two bright branches, which unambiguously demonstrates that NFRHT is predominated by identity of a drift-biased graphitelike structure. If N increases to 35, phototunneling coefficients $\xi(\omega, k_x, k_y)$ form multiple bright bands. However, due to interference in the compact system, surface states only weakly couple in a small area, dramatically reducing the number of modes that effectively participate in heat exchange, and thereby dramatically reducing the total integrated flux. In this case, the flux is only $h = 3.1\,\mathrm{kW\,m^{-2}\,K^{-1}}$, as shown in Fig. 6(b). Figure 8(b) shows $\xi(\omega, k_x, k_y)$ with an optimum d_i. Compared with the scenario in Fig. 8(a), all the NSPP branches of each drift-biased graphene layer are close to each other and very strong. Clearly, the two bright,
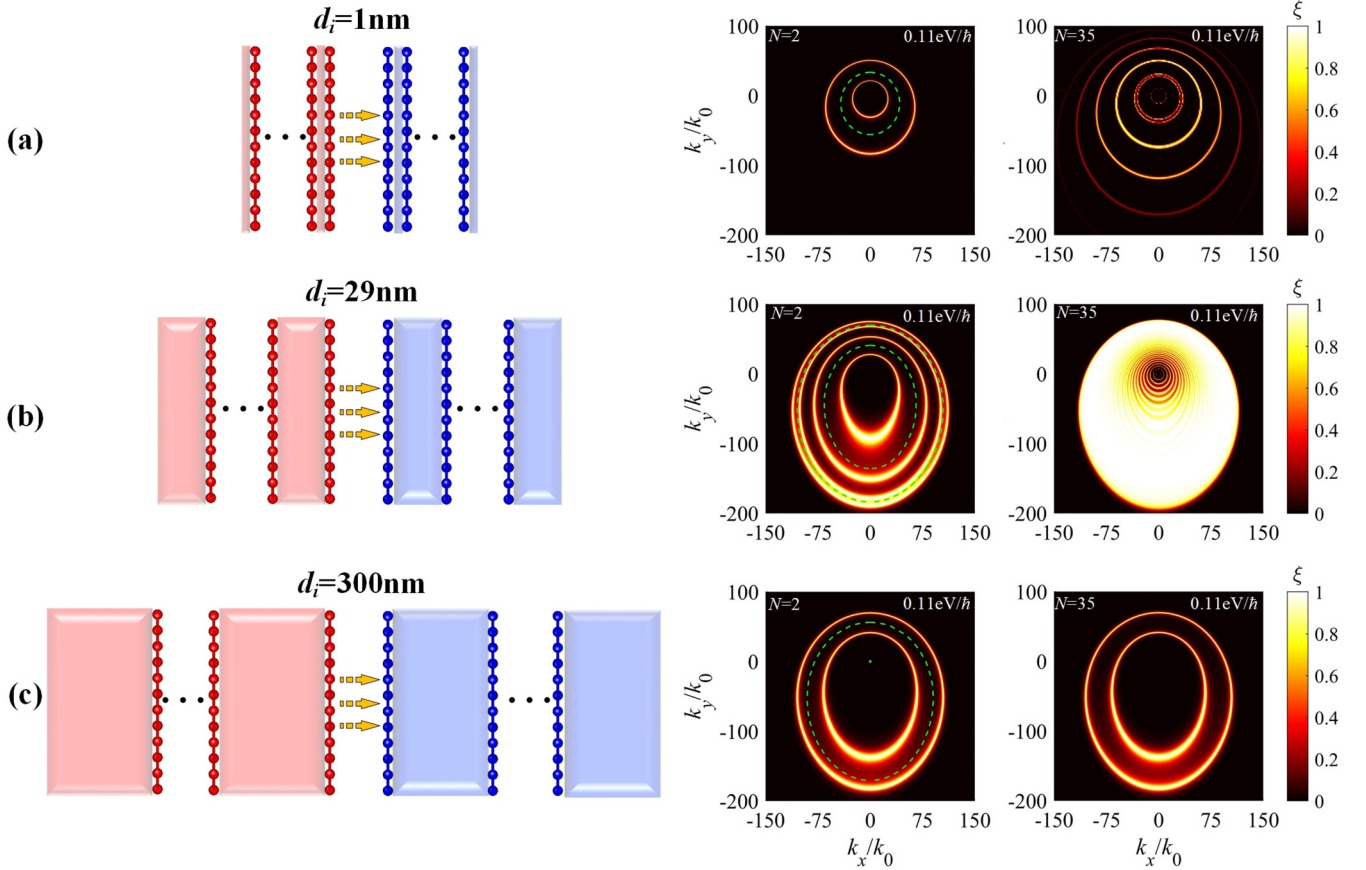
FIG. 8. Photonic-transmission coefficient contours for multilayers of three different thicknesses at a frequency of 0.11 eV/$\hbar$: (a) $d_i = 1$ nm, (b) $d_i = 29$ nm, and (c) $d_i = 300$ nm nm for $N = 2$ and 35. The middle gap width is fixed at $d_0 = 30$ nm. The green dashed line for $N = 2$ corresponds to the dispersion curve, as determined by Eq. (12).

coupled branches contributed by the graphene sheets of the first graphene layer still appear; the NSPP branches provided by the additional graphene layers are located inside the two branches supported by the first graphene layer. The double green dotted lines are located between the bright branches, which unambiguously demonstrates that NFRHT is predominated by the double NSPPs of the bilayer system. When N increases to 35, a large, bright, egg-shaped area with a PTC value close to 1 is formed in wave-vector space, i.e., all the NSPP branches of drift-biased graphene layers merge together. Thus, the heat-transfer coefficient dramatically increases, and in this case, $h = 24.9$ kW m^{-2} K^{-1}. For d_i higher than the optimum value, due to the strong attenuation caused by dielectric spacer with large thickness, the dielectric spacer filters the additional branches. In Fig. 8(c), for $N = 2$, the two coupled, bright branches contributed by the graphene sheets of the first layer are observed, while the NSPP branches provided by the additional graphene layers disappear. The dispersion curve provided by the second layers also degrades into to a green dot. As the number of graphene layers increases, the photon-tunneling probabilities are unchanged, i.e., the additional layers do not contribute to NFRHT.

To elucidate the above analysis and the influence of structural parameters on the enhanced effect of the nonreciprocal multilayer, Fig. 9(a) shows the heat-transfer enhancement

ratio R between multilayers with a high current velocity of $0.9v_f$ and a monolayer without drift current as a function of vacuum gap and thickness of the dielectric spacer. The green line divides the contour into the suppressed ($R < 1$) and
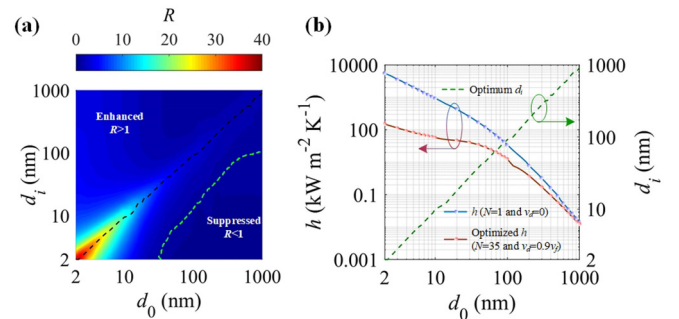

FIG. 9. (a) Heat-transfer enhancement ratio R between drift-biased multilayers and monolayer without current as a function of vacuum gap and thickness of dielectric spacer. The black line corresponds to maximum R. The green line divides the contour into the suppressed ($R < 1$) and the enhanced ($R > 1$) heat-transfer regions. (b) The optimized heat-transfer coefficient h, and the corresponding optimum d_i as a function of d_0.
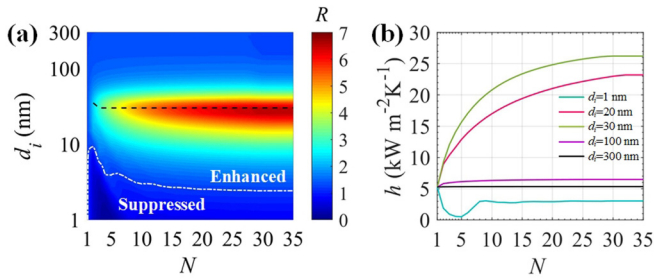
FIG. 10. (a) Heat-transfer enhancement ratio R between drift-biased multilayers and monolayer without current as a function of N and d_i. (b) Radiative-heat coefficient with respect to N for $d_i = 1$, 20, 30, 100, and 300 nm. The gap width is taken as $d_0 = 30$ nm. In (a), the black line corresponds to the maximum ratio, and the white dashed line divides the contour into the suppressed ($R < 1$) and the enhanced ($R > 1$) heat-transfer regions.

the enhanced ($R > 1$) heat-transfer regions. When $d_i \ll d_0$, an apparent suppression in heat transfer is observed in the multilayers, especially for a large vacuum gap d_0. For instance, for $d_i = 2$ nm and $d_0 = 1$ μm, R decreases to 0.14; for small values of d_0 and large thicknesses of d_i, compared with the case of the monolayer, the heat-transfer enhancement of the multilayer is significant due to NSPPs supported by the first layer of drift-biased graphene. As the vacuum gap d_0 increases, due to the ultraconfined and lossy character of NSPPs, the NSPPs supported by the first layer of drift-biased graphene are filtered by free space, resulting in a weak enhancement of heat transfer. The black line corresponds to the maximum ratio in Fig. 9(a). As $d_0 \approx d_i$, the ratio is maximal. For the nonreciprocal multilayers, the relay mechanism works best when d_0 is comparable to the thickness of the dielectric spacer, similar to the optimum condition for the geometry that exhibits the superlens effect [47]. Moreover, the enhancement on NFRHT is much stronger at the smaller vacuum gap. For instance, R approaches 36.5 at $d_0 = 2$ nm but 1.2 at $d_0 = 1$ μm. Figure 9(b) shows the optimum h and the corresponding optimum thickness d_i as a function of the vacuum gap d_0. When the vacuum gap d_0 is small, a more compact multilayer structure is expected to produce larger h and a higher enhanced effect R. In contrast, for large gap widths, the optimum structure requires a thicker dielectric spacer. To maintain a maximum heat-transfer rate for all vacuum gaps, one can thus develop a dynamical control system to vary the thickness of the dielectric spacer in sync with the gap width. Moreover, as gap width increases, the RHTC of the multilayers tends to that of a single-layer graphene sheet, without drift current, due to the ultraconfined and lossy character of the NSPPs.

To examine the effects of the number of graphene layers and the thickness of the dielectric spacer on radiative heat transfer, Fig. 10(a) shows the heat-transfer enhancement ratio R between multilayers with a high drift-current velocity of $0.9v_f$ and a monolayer without current as a function of N and d_i in. The vacuum gap is taken as $d_0 = 30$ nm. Not surprisingly, when enough graphene sheets are stacked, the

heat-transfer coefficient remains unchanged. The predicted enhanced and suppressed regions are consistent with the above analysis. Figure 10(b) shows h as a function of the number of graphene layers for $d_i = 1$, 10, 20, 30, 100, and 300 nm. Interestingly, when d_i is far smaller than d_0, with an increasing number of graphene layers, h decreases at first and then increases. The decrease in h for a few-layers system can be understood as follows: as discussed above, since $d_i \ll d_0$, the surface states only weakly couple in a small region, effectively suppressing the modes from participating in heat exchange. This phenomenon is more pronounced when there are fewer layers. With an increasing number of graphene layers, new NSPP states appear. This result is consistent with the photonic transmission coefficient diagram of Fig. 8(a). These newly added surface states make SPP coupling more effective, thereby increasing h. For large thicknesses of dielectric spacer, as the number of graphene layers increases, the radiative heat transfer shows a monotonous growth trend. However, when the thickness is greater than the optimum value, the evanescent wave of the newly added layer is strongly attenuated before reaching the surface of the other multilayer system; hence, the enhanced rate of NFRHT gradually decreases.

V. CONCLUSIONS

We studied the NFRHT and active modulation of heat transfer close to an anisotropic multilayer that supports multiple nonreciprocal SPPs (MNSPPs). The MNSPP topology of the anisotropic metasurface could be tuned by the drift current. In our configuration, due to the excitation of and interference among anisotropic surface waves, NFRHT can be significantly amplified more than 36 times compared with the case of a monolayer without a drift current. We analyzed the dependence of the RHTC on the number of graphene layers, the drift-current velocity, the chemical potential, the vacuum gap, and the thickness of the dielectric spacer. The heat-transfer rate can be modulated over considerably and can even be reduced below that in monolayer systems without a drift current through the adjustment of thicknesses of dielectric spacer and vacuum gap. The physics are interpreted qualitatively by analyzing the distribution of the photonic-transmission coefficient, plasmon dispersions, and penetration depth, clearly highlighting the role on NFRHT played by the anisotropic surface mode. Our work represents the first step in the study of energy exchange mediated by an anisotropic metasurface multilayer structure. Moreover, it is expected to provide a more powerful way to enhance energy transport using multiple anisotropy plasmons. Our work opens the door to exploring the anisotropic optical properties of metasurfaces based on measured heat-transfer properties.

[1] J. R. Howell, R. Siegel, and M. P. Menguc, *Thermal Radiation Heat Transfer*, 5th ed. (Taylor and Francis, New York, 2010).

[2] Y. C. Zhang, W. B. Rossow, A. A. Lacis, V. Oinas, and M. I. Mishchenko, J. Geophys. Res-Atmos **109**, D19105 (2004).

[3] D. Polder and M. Van Hove, Phys. Rev. B **4**, 3303 (1971).

[4] Z. M. Zhang, *Nano/Microscale Heat Transfer* (McGraw-Hill, New York, 2007).

[5] V. Fernández-Hurtado, F. J. García-Vidal, S. H. Fan, and J. C. Cuevas, Phys. Rev. Lett. **118**, 203901 (2017).

[6] O. Ilic, M. Jablan, J. D. Joannopoulos, I. Celanovic, H. Buljan, and M. Soljacic, Opt. Express. **20**, A366 (2012).

[7] R. Q. Wang, J. C. Lu, and J. H. Jiang, Phys. Rev. Appl. **12**, 044038 (2019).

[8] D. D. Feng, E. J. Tervo, S. K. Yee, and Z. M. Zhang, Nanosc. Microsc. Therm. **24**, 1 (2020).

[9] L. X. Zhu, A. Fiorino, D. Thompson, R. Mittapally, E. Meyhofer, and P. Reddy, Nature (London) **566**, 239 (2019).

[10] K. F. Chen, P. Santhanam, and S. H. Fan, Phys. Rev. Appl. **6**, 024014 (2016).

[11] X. L. Liu and Z. M. Zhang, Nano. Energy. **26**, 353, (2016).

[12] C. R. Otey, W. T. Lau, and S. Fan, Phys. Rev. Lett. **104**, 154301 (2010).

[13] P. Ben-Abdallah and S.-A. Biehs, Phys. Rev. Lett. **112**, 044301 (2014).

[14] Y. Zhang, C. L. Zhou, H. L. Yi, and H. P. Tan, Phys. Rev. Appl. **13**, 034021 (2020).

[15] V. Kubytskyi, S.-A. Biehs, and P. Ben-Abdallah, Phys. Rev. Lett. **113**, 074301 (2014).

[16] S. Shen, A. Narayanaswamy, and G. Chen, Nano Lett. **9**, 2909 (2009).

[17] M. Francoeur, M. P. Menguc, and R. Vaillon, Appl. Phys. Lett. **93**, 043109 (2008).

[18] O. Ilic, M. Jablan, J. D. Joannopoulos, I. Celanovic, H. Buljan, and M. Soljacic, Phys. Rev. B **85**, 155422 (2012).

[19] K. Asheichyk, B. Müller, and M. Krüger, Phys. Rev. B **96**, 155402 (2017).

[20] K. Asheichyk and M. Krüger, Phys. Rev. B **98**, 195401 (2018).

[21] H. Iizuka and S. Fan, Phys. Rev. Lett. **120**, 063901 (2018).

[22] Y. H. Kan, C. Y. Zhao, and Z. M. Zhang, Phys. Rev. Appl. **13**, 014069 (2020).

[23] R. Messina, P. Ben-Abdallah, B. Guizal, and M. Antezza, Phys. Rev. B **96**, 045402 (2017).

[24] B. Zhao, B. Guizal, Z. M. Zhang, S. Fan, and M. Antezza, Phys. Rev. B **95**, 245437 (2017).

[25] K. Z. Shi, F. L. Bao, and S. L. He, ACS Photon. **4**, 971 (2017).

[26] Y. Zhang, C. H. Wang, H. L. Yi, and H. P. Tan, J. Quant. Spectrosc. Radiat. Transfer **221**, 138 (2018).

[27] X. L. Liu and Z. M. Zhang, Appl. Phys. Lett. **107**, 143114 (2015).

[28] X. Wu, C. Fu, and Z. M. Zhang, J. Heat Transfer **147**, 072802 (2020).

[29] H. Salihoglu and X. F. Xu, J. Quant. Spectrosc. Radiat. Transfer **222**, 115 (2019).

[30] Y. Zhang, C. L. Zhou, L. Qu, and H. L. Yi, Appl. Phys. Lett. **116**, 151101 (2020).

[31] X. L. Liu, J. D. Shen, and Y. M. Xuan, Nanosc. Microsc. Therm. **23**, 188 (2019).

[32] L. X. Ge, Z. J. Xu, Y. P. Cang, and K.Opt. Express. **27**, A1109 (2019).

[33] H. H. Wu, Y. Huang, L. J. Cui, and K. Y. Zhu, Phys. Rev. Appl. **11**, 054020 (2019).

[34] L. X. Ge, K. Gong, Y. P. Cang, Y. S. Luo, X. Shi, and Y. Wu, Phys. Rev. B **100**, 035414 (2019).

[35] T. A. Morgado and M. G. Silveirinha, ACS Photonics **5**, 4253 (2018).

[36] T. A. Morgado and M. G. Silveirinha, Phys. Rev. Lett. **119**, 133901 (2017).

[37] G. Lovat, G. W. Hanson, R. Araneo, and P. Burghignoli, Phys. Rev. B **87**, 115429 (2013).

[38] F. V. Ramirez, S. Shen, and A. J. H. McGaughey, Phys. Rev. B **96**, 165427 (2017).

[39] V. E. Dorgan, M.-H. Bae, and E. Pop, Appl. Phys. Lett. **97**, 082112 (2010).

[40] H. Ramamoorthy, R. Somphonsane, J. Radice, G. He, C. P. Kwan, and J. P Bird, Nano Lett. **16**, 399 (2016).

[41] J. S. Gomez-Diaz, M. Tymchenko, and A. Alù, Opt. Mater. Express. **5**, 2313 (2015).

[42] M. Nakayama, J. Phys. Soc. Jpn. **36**, 393 (1974).

[43] K. W. Chiu and J. J. Quinn, Phys. Rev. B **9**, 4724 (1974).

[44] O. V. Kotov and Y. E. Lozovik, Phys. Rev. B **100**, 165424 (2019).

[45] T. Zhan, X. Shi, Y. Dai, X. Liu, and J. Zi, J. Phys.: Condens. Matter. **25**, 215301 (2013).

[46] P. Yeh, J. Opt. Soc. Am. **69**, 742 (1979).

[47] V. E. Dorgan, A. Behnam, H. J. Conley, K. I. Bolotin, and E. Pop, Nano Lett. **13**, 4581 (2013).

[48] J. B. Pendry, Phys. Rev. Lett. **85**, 3966 (2000).

[49] R. Messina, M. Antezza, and P. Ben-Abdallah, Phys. Rev. Lett. **109**, 244302 (2012).